

Monolayer Suppression of Transport Imaged in Annealed PbSe Nanocrystal Arrays

Michael D. Fischbein,[†] Matthew Puster,^{†,‡} and Marija Drndic^{*,†}

[†]Department of Physics and Astronomy, University of Pennsylvania, Philadelphia, Pennsylvania, 19104 and

[‡]Department of Materials Science and Engineering, University of Pennsylvania, Philadelphia, PA 19104

ABSTRACT We use correlated electrostatic force, transmission electron, and atomic force microscopy (EFM, TEM, and AFM) to visualize charge transport in monolayers and up to five layers of PbSe nanocrystal arrays drop-cast on electrode devices. Charge imaging reveals that current paths are dependent on the locally varying thickness and continuity of an array. Nanocrystal monolayers show suppressed conduction compared to bilayers and other multilayers, suggesting a departure from linear scaling of conductivity with array thickness. Moreover, multilayer regions appear electrically isolated if connected solely by a monolayer. Partial suppression is also observed within multilayer regions that contain narrow junctions only several nanocrystals wide. High-resolution TEM structural imaging of the measured devices reveals a larger reduction of inter-nanocrystal spacing in multilayers compared to monolayers upon vacuum-annealing, offering a likely explanation for the difference in conductivity between these two cases. This restriction of transport by monolayers and narrow junctions is an important factor that must be addressed in future designs of optoelectronic devices based on nanocrystals.

KEYWORDS PbSe, nanocrystals, charge transport, annealing, electrostatic force microscopy

Arrays formed by self-assembled semiconductor nanocrystal (NC) quantum dots are compelling as both model systems to study artificial solids with controllable Hamiltonians described by the Hubbard model and as tunable platforms for electrical, thermal and optical applications.¹ Progress on both of these fronts requires a solid understanding and control over their charge transport properties, and over the past decade significant advancement has been achieved in revealing and manipulating the fundamental processes governing these systems.^{2,3} However, the role of assembly disorder and local thickness variations in contributing or inhibiting current through the arrays has not been well established.

NC arrays have been generally found to be in the weak inter-dot coupling regime and conventional current–voltage (I – V) measurements on untreated NC arrays in electrode gap devices have shown them to be highly resistive, with or without photoexcitation. Thermal annealing at moderate temperatures and chemical treatments have been shown to dramatically increase conduction in these arrays by increasing inter-dot coupling.^{4–21} Despite these advances, there still remain the outstanding issues of how various NC array properties scale with the number of NC layers and, ultimately, what the practical thickness limits are with regard to performance in a device configuration. For example, NC monolayers were found to be more efficient than multilayers for electroluminescence applications in sandwich geometry devices resulting from inefficient radiative recombination

processes in multilayers attributed to charge trapping on the quantum dot sites and overall inhibited charge conduction.²² In contrast, NC transistor behavior in planar geometries has been realized only in thicker films with tens of layers.^{5,7,17} In such transport studies it remains to be established whether the first monolayer adjacent to the substrate carries most of the current compared to the rest of the film, as might be expected from simple arguments of capacitor charging.⁵ Previous measurements in CdSe nanocrystal arrays found the assumption of current proportionality with film thickness to be only partly successful in explaining transport data, showing a deviation of the voltage dependence of current transients in the thin film regime at around 20 layers.²³ So far, film thickness and device size scaling of NC array conductivity remains an open question that is particularly interesting as the two-dimensional limit is approached.

While traditional transport measurements reveal the global or averaged electronic properties and can overlook microscopic variations, scanning probe methods are more suitable to directly measure the local parameters, such as inter-NC barriers and spacing, and address their effects on macroscopic behavior.^{6,24–26} For example, delocalization of electron and hole wave functions across neighboring NCs has been observed in scanning-tunneling currents measured in vacuum-annealed PbSe NC arrays on conducting substrates.²⁵ Correlated atomic-force, electrostatic-force, and transmission-electron microscopy (AFM, EFM, and TEM) offers high-resolution spatial mapping of the charge distribution in NC arrays over large areas of a device as a function of the electric field generated by the device electrodes. We have previously used this imaging approach to reveal local variations in the charge distribution in NC arrays in a device

* To whom correspondence should be addressed. E-mail: drndic@physics.upenn.edu. Phone: 215-898-5810. Fax: 215-898-2010.

Received for review: 03/10/2010

Published on Web: 05/14/2010

configuration and map them to nanometer-scale array discontinuities.⁶

In this Letter, we report on applying combined microscopy (AFM/EFM/TEM) on *in situ* vacuum-annealed PbSe NC arrays within two-terminal electrode geometries that locally vary in thickness from monolayers up to five layers. We observe strong suppression of EFM signals in monolayer regions and generally find that monolayers are insulating. We also scan complex networks of superlattices that branch throughout a fragmented monolayer background and find that multilayer regions connected solely via a monolayer region are electrically isolated, further demonstrating the insulating behavior of monolayers. High-resolution TEM imaging of these devices shows that NCs in multilayer regions become more closely packed due to annealing than NCs in monolayer regions, consistent with the contrast in charging efficiency. Small variations of inter-particle spacing can lead to large variation of tunneling probabilities across the arrays, thus offering a likely explanation of the observed effects.

EFM has been employed in various manifestations to study spatially dependent electronic characteristics in nanostructures.^{26–29} We used an established DC-EFM method^{30,31} in our study of NC arrays, where a conductive AFM tip is used to first measure the topography (tapping mode) of NC arrays between electrodes and then rescan the same area at a fixed height above the surface to measure shifts in the cantilever oscillations, which yield information regarding electrostatic forces acting on the tip.⁶ The EFM scanning mode records either the frequency shift, $\Delta\nu$, or the phase shift, $\Delta\phi$, of the cantilever. These images can be scaled onto one another through the relation $\Delta\phi \sim (2Q/\nu_o)\Delta\nu$, where ν_o is the cantilever resonance frequency and Q is the quality factor.^{30,31} Though a fully accurate quantitative analysis of the EFM signals is complicated due to convoluted effects of capacitive coupling between the tip and the sample, together with the effects of static charges and the particular details of the tip and sample geometries,³⁰ the EFM images nevertheless allow one to clearly distinguish between NC array regions of higher or lower capacity for charge transport.

The AFM used in this EFM study of PbSe NCs was a Veeco EnviroScope, which offers an environmentally controlled sample chamber that allows samples to be kept under vacuum or inert gas flow to minimize oxidation. Two-terminal $\sim 1.5 \times 1 \mu\text{m}^2$ large electrode gaps were fabricated on the 40 nm thick SiN_x membrane window regions of etched SiN_x/Si+ chips using electron beam lithography and metal evaporation of a 30 nm Au layer on top of a 3 nm Ni adhesion layer.³² Up to six gaps were patterned onto each chip within the $\sim 50 \times 50 \mu\text{m}^2$ window region. Voltages were applied to device electrodes with a LabVIEW controlled Yokogawa DC power supply connected through a BNC breakout box to a socket on the back of the AFM sample chamber. Devices were wire bonded to terminals on the stage that were themselves wired to a PCB insert that

plugged into the AFM socket. Standard $I-V$ measurements could be performed in parallel to EFM scanning, but leakage currents in the AFM hardware made low-level (<20 pA) current measurements impossible. In addition to providing compatible surfaces for high-resolution TEM imaging, the use of suspended SiN_x window devices eliminated undesirable contributions to the EFM signals otherwise possible in devices with underlying Si substrates, such as screening of the sample by the doped Si substrate and effects caused by charges typically located at the dielectric/Si interface. PbSe NCs, 6.8 nm in diameter ($<5\%$ size dispersion), with ~ 2 nm oleic acid capping were drop-cast from a diluted 9:1 hexane/octane solvent onto the devices. Before drop-casting, all bare devices were imaged with EFM at a range of electrode voltages (fields up to $\sim 10^7$ V/m) to ensure that substrate charging did not contribute to the background EFM signal (see Figure S1 in Supporting Information). Immediately after drop-casting the NCs, devices were placed into the AFM measurement chamber, which was then quickly evacuated to pressures $<10^{-5}$ Torr. Exposure of NCs to air was kept under ~ 2 min to minimize oxidation or degradation of the NCs. Similar drop-casting and drying procedures have been also used in many NC transport measurements to date.^{4,5,11–15,15,21,23,32,33} As-deposited PbSe NC arrays were first imaged with EFM and subsequently annealed under vacuum to 130 °C. After slowly cooling to room temperature, EFM studies were carried out under N₂ gas for a range of voltages applied to device electrodes. Only postanneal imaging yielded appreciable charging signals from the NCs, without requiring prolonged voltage exposure⁶ to induce slow charging (see Figure S2 in Supporting Information). Tips used for EFM imaging were Antimony n-doped Si coated with 20 nm Pt/Ir on top of 3 nm Cr. The cantilevers had resonance frequencies $\nu_o = 60–100$ Hz and spring constants $k = 1–5$ N/m. Images were acquired at a 1 Hz scan rate with tip–surface distances ranging from 10–50 nm for the EFM scans. After the EFM measurements were completed, samples were imaged with a JEOL 2010F TEM operating at 200 kV.

Figure 1a shows an AFM height scan of an electrode pair after depositing PbSe NCs and annealing the device in vacuum at 130 °C for ~ 12 h. As seen in the image, the PbSe NC film ranges in thickness from approximately 1 to 5 NC layers and is highly structured. TEM imaging of the device revealed that the NCs assembled into complex networks of superlattices (Figure 1c,d) branching throughout a fragmented monolayer background. The formation of the superlattice network structure, which extended throughout the membrane surface, was facilitated by rapidly reducing the chamber pressure to $\sim 10^{-4}$ Torr immediately after drop-casting to increase the solvent evaporation rate and was not altered noticeably by annealing. In contrast, we observe that slower drying conditions at atmospheric pressures result in more uniform structures. Complex nanocrystal assembly patterns form during the nonequilibrium drying dynamics

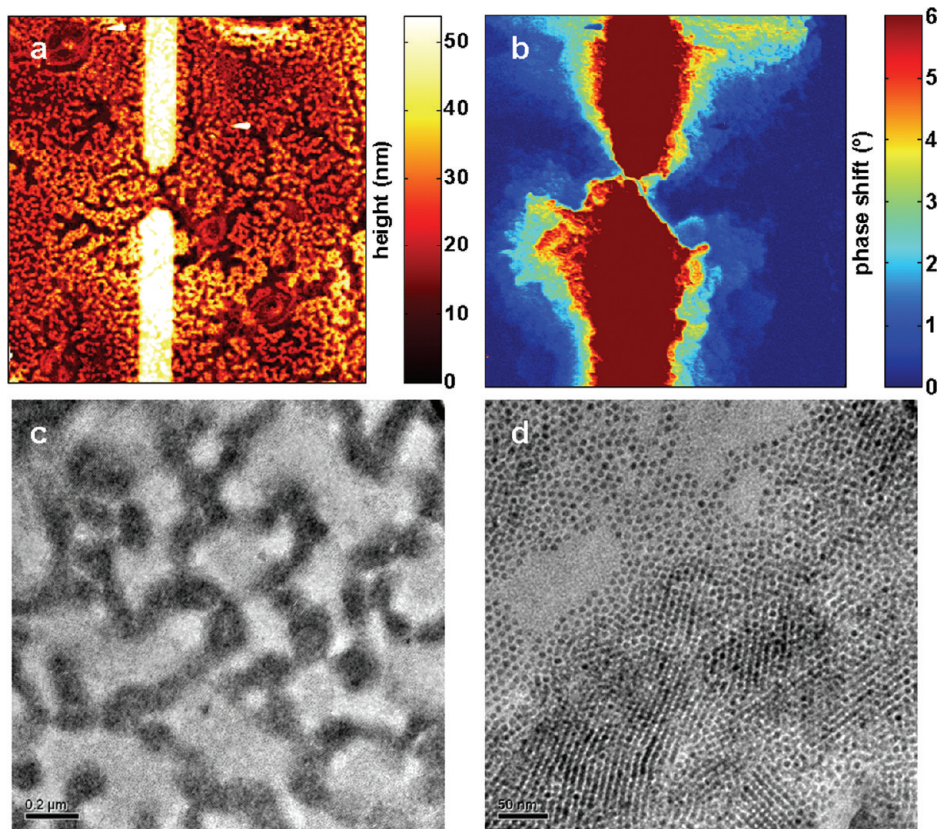


FIGURE 1. (a) Height image ($15 \times 15 \mu\text{m}^2$ scan) of an electrode gap with a nonuniform annealed film of 6.8 nm PbSe NCs distributed across the surface. (b) An EFM (phase) image ($15 \times 15 \mu\text{m}^2$) taken of this gap corresponding to 5 V applied to the upper electrode and -5 V applied to the lower electrode. (c) TEM image showing superlattice (dark regions) branching across a monolayer background (scale bar = 200 nm). (d) TEM image showing interface between NC superlattice and monolayer (scale bar = 50 nm).

of an evaporating solvent upon drop-casting³⁴ and they offer a convenient means for probing the influence of array thickness on conductivity within a single device. Figure 1b shows the corresponding EFM (phase) image for this electrode gap, taken immediately after applying 5 V to the upper electrode and -5 V to the lower, while keeping the AFM tip, other metal features on the Si⁺ substrate, and the Si⁺ at 0 V. This measurement configuration achieves an electric field of $\sim 7 \times 10^6$ V/m in the gap region, compared to an order of magnitude lower field ($\sim 5 \times 10^5$ V/m) from these electrodes to other neighboring grounded electrode pairs on the chip surface. It should be noted that the dominant term in the EFM signal is proportional to $(V_{\text{sample}} - V_{\text{tip}})^2 = V_{\text{sample}}^2$, since $V_{\text{tip}} = 0$ V in our case and is therefore mostly sensitive to the voltage magnitude and not polarity.^{30,31} Furthermore, because the electrostatic force on the tip is always attractive, the phase and frequency shifts are displayed as magnitudes. The highly branched structure in the EFM image is well correlated with the cluster-network topography of the NC film seen in the height image. EFM images for a range of other voltages applied displaying the EFM signal evolution with increasing electric field are shown in Figure S3 in the Supporting Information. Figure S4 in the Supporting Information shows additional AFM and EFM scans of another

electrode pair on the same chip surface, displaying a similar example of a branched structure in the EFM signal.

TEM characterization of electrode gaps revealed further insight into the role of NC film structure in charging behavior and was critical for identifying transport suppression by monolayer regions. Figure 2 focuses on the area around the upper-right edge of the lower electrode shown in Figure 1a,b. This region was chosen for detailed analysis because of the high degree of local structure seen in its corresponding EFM image. Figure 2a,b shows magnified AFM and EFM images of this area. Topographic structure can be seen to correlate strongly with EFM features, though there are many NC structures in the height image that do not appear strongly in the EFM image. One important observation is that there are multilayer structures through which charge does not propagate even though they seem structurally well connected to the voltage source. The suppression of charge propagation into these regions may have a number of reasons including larger density of local charge traps in the NCs, the substrate or at interfaces, larger local disorder and larger offsets in neighboring NC energy levels, and energy barrier bottlenecks along conduction paths that cannot be overcome at the field strengths applied in this study. EFM and TEM imaging however did not clearly reveal static

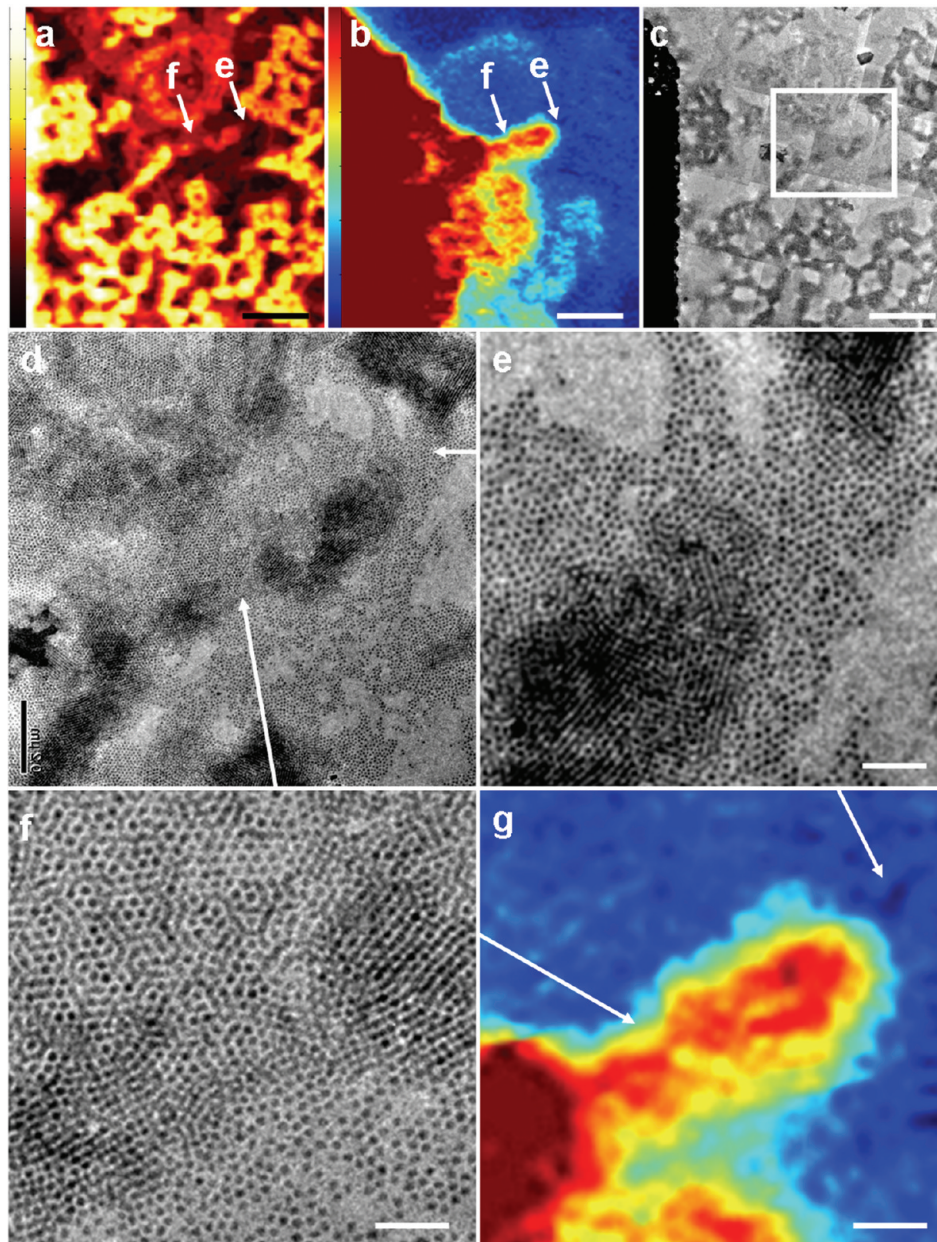


FIGURE 2. (a) Height image of a region along the right edge of the lower electrode shown in Figure 1a, where the highly structured PbSe NC film is in direct contact (height scale: 0 nm (black) to 55 nm (white)). Portions of the height structure match structure in (b) the corresponding EFM (phase) image (phase shift scale: 0 (blue) to 3° (red)). (c) A collection of about 25 TEM images taken in this same region and sewn together to recreate the full area seen in (a) and (b). The edge of the electrode appears as the black slab (image left). The darker gray regions in the TEM image correspond to the NC superlattice networks and the patterns match the AFM and EFM structure. (d) Higher-magnification TEM image of the middle of the region in (c). (e,f) TEM zoom-in corresponding to the regions indicated by arrows in (a,b,d). Charge was able to propagate through the few-layer channel (f) but not through the monolayer (e). (g) EFM image of the same area shown in (d). Scale bars are 500, 500, 500, 200, 50, 50, and 200 nm from (a) to (g).

charges in these regions or obvious structural differences. More sensitive probing methods are therefore needed to fully understand all of the factors responsible for restricting transport in regions expected to be conducting based on the structural (AFM and TEM) characterization only. However, the role of monolayers in the suppression of transport was revealed by correlated imaging. Figure 2c shows a collection of roughly 25 TEM images that were sewn together to recreate the full region ($\sim 4.5 \times 4.5 \mu\text{m}^2$) shown in the

corresponding AFM and EFM images. The electrode edge can be seen as the large dark structure along the left edge of the TEM image. Figure 2d shows a higher magnification TEM image of a region corresponding to the middle of the EFM image, where a fingerlike charged structure is seen extending $\sim 25^\circ$ upward and to the right. Figure 2g shows the corresponding EFM image of this region, magnified from Figure 2b. The TEM image shows that this charged structure is a ~ 150 nm wide superlattice that extends $\sim 1 \mu\text{m}$ from

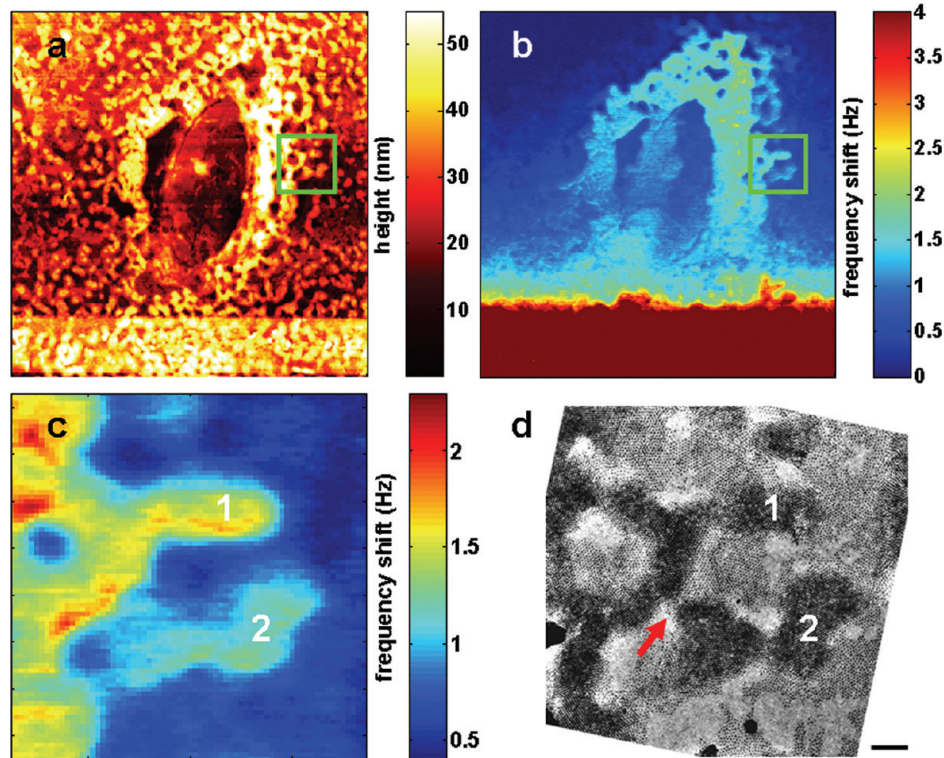


FIGURE 3. (a) Height image ($8 \times 8 \mu\text{m}^2$ scan) of 6.8 nm PbSe NCs assembled in a complex pattern, touching a horizontal electrode (bottom of the image). (b) Corresponding EFM image (frequency shift) with the electrode at -5 V . (c) Zoom-in of the EFM image in (b) in the region indicated by green squares in (a,b), showing two regions (1 and 2) that are of roughly equivalent height but different EFM signal. (d) TEM image showing NC bottleneck (red arrow) that is responsible for the reduced EFM signal in region 2. (Scale bar = 100 nm.)

the lower-left corner of the image. Along its length, the height varies between ~ 16 and $\sim 25 \text{ nm}$, corresponding to approximately 2 and 3 NC layers. Comparison with the EFM image shows that charging was significantly interrupted by the transition from multilayers to monolayer (Figure 2e). Furthermore, another adjacent superlattice region in the upper-right region of the TEM image does not appear charged in the EFM image even though it is directly connected by monolayer patches to the highly charged superlattice. These observations indicate that charge transport through NC monolayer regions is very inefficient. In contrast, nearby regions only 2 and 3 NC layers thick became significantly charged, as demonstrated in Figure 2f. Correlated image analysis of over 30 regions displaying strong EFM features revealed conclusively that monolayer regions are a significant source of transport restriction. In this analysis, we never observed clear evidence of propagation of charge into a monolayer region, whereas in most cases we observed efficient charge propagation in multilayer regions. In cases where propagation in multilayers was poor, it was usually attributable to weak coupling between the multilayer region and any neighboring charged regions, as the example shown in Figure 3 demonstrates.

Figure 3 shows evidence that, in addition to array thickness, array width is an important factor in the limitation of charge propagation if the width is sufficiently small. Figure 3a shows the height image of NCs assembled into various

shapes and thicknesses, where a complex assembly structure is coupled strongly to an electrode at -5 V , as demonstrated by the EFM image of the same region in Figure 3b. Figure 3c shows a zoom in of the EFM signal from a region of this array structure enclosed by the indicating squares in Figure 3a,b, where the multilayer is roughly “C” shaped. Interestingly, the upper and lower halves of the shape are of roughly the same height, $\sim 3\text{--}4$ NC layers thick, but different EFM signal strength. These are labeled as regions 1 and 2 in Figure 3c. Figure 3d shows the corresponding TEM image of this region. As indicated in the TEM image, the lower region (region 2) is weakly connected to the larger array structure through a narrow bottleneck only several NCs wide, marked by the red arrow in Figure 3d, whereas the upper region (region 1) is significantly better coupled to the larger array through a junction over 10 NCs wide, and therefore also to the energized electrode. This effect of bottlenecks limiting the propagation of charge is seen in a large number of cases across the measured devices and largely explains the suppressed propagation of charge in regions that are not limited by monolayers. Another example of a 7 NC-wide transport bottleneck between two $\sim 5 \text{ nm}$ thick superlattice regions in a different, parallel-plate electrode geometry containing mostly highly ordered hexagonally packed domains is shown in Figure S5 in the Supporting Information. This example also demonstrates that charge propagation was not hindered across superlattice

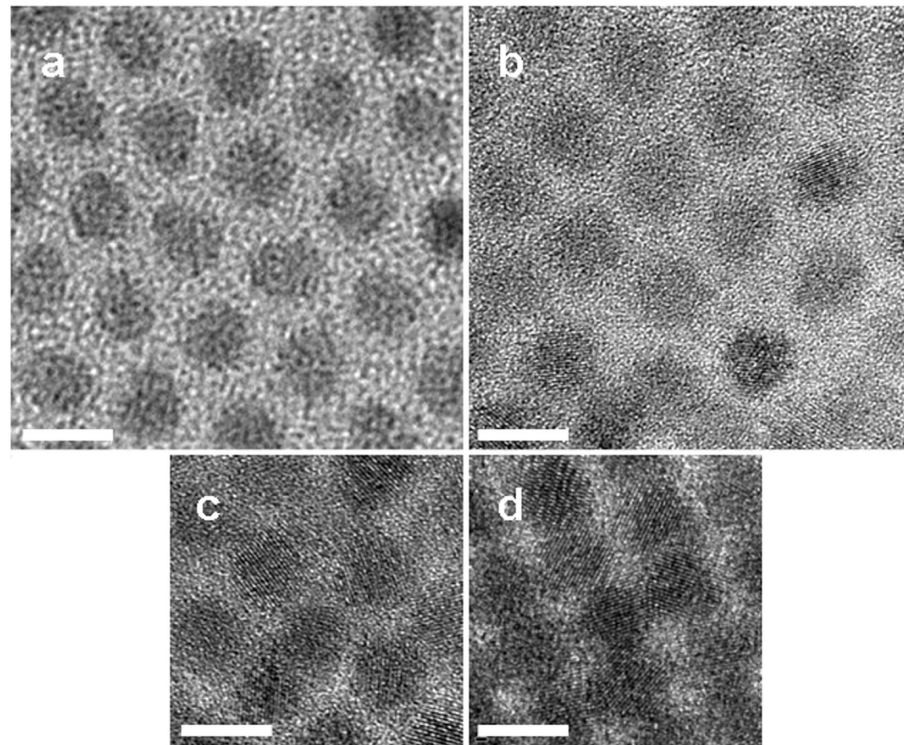


FIGURE 4. (a) TEM image of the PbSe NCs, as-deposited. (b) TEM image taken of PbSe NCs on the device after annealing at 130 °C, showing reduced inter-NC spacing. (c,d) Multilayers (2–3 layers) of well-ordered PbSe NCs after annealing showing substantially reduced inter-NC spacing. The lattice orientations of individual NCs can be seen. Scale bars are all 10 nm.

domain boundaries and the domains coupled electrically to the metal electrodes regardless of their specific domain orientation relative to the electrodes (see Supporting Information Figure S5a).

To investigate the origins of transport suppression by monolayer regions, we used high-resolution structural imaging of the measured devices to inspect the variation of inter-dot separations and interfacial boundaries between different regions of the NC film. By zooming-in to the single-particle level with the TEM, it is possible to observe that NCs in the multilayer regions became more closely packed due to annealing than the NCs in the monolayer regions, consistent with the contrast in charging efficiency. Because the tunneling probability increases exponentially as the inter-particle spacing decreases,⁴ small variations of inter-particle spacing in the array can have a large effect on the overall transport. For example, a decrease of inter-particle separations, that is, the widths of the tunneling barriers, by 0.6 nm in CdSe NC arrays is expected to increase the tunneling probability by a factor of ~400.⁴ Figure 4a shows a PbSe NC monolayer as-deposited, before annealing. The inter-NC spacing is ~2.5 nm on average in an unconstrained monolayer, larger than the nominal length of the ligand molecules (2 nm). Figure 4b–d shows TEM images of monolayers and multilayers on the device surface after annealing at 130 °C for 12 h. Figure 4b shows that the annealing treatment did reduce the inter-NC spacing, down to ~1.8 nm on average. The remaining images show that the inter-NC spacing was reduced much

more significantly in multilayer regions to under 1 nm. We note that NCs retain a high degree of crystallinity after annealing and lattice orientations are clearly visible in TEM images (Figure 4c,d and Figure S6 in the Supporting Information). The enhanced reduction of NC spacing in multilayers compared to monolayers offers a likely explanation for the difference in conductivity between the two cases. TEM images in Figures 1d and 2e,f show several examples of interfaces between NC superlattices and monolayers. Because of the long-range of the Coulomb interactions that make up the EFM signals, the edges of charged regions appear to blur beyond their true spatial extent on the order of 100 nm. Consequently, the resolution of EFM is insufficient to rule out the possibility of limited charge propagation across multilayer–monolayer interfaces.

In conclusion, correlated transport (EFM) and structural (AFM and TEM) imaging of PbSe NC arrays in electrode devices shows that monolayer regions and narrow array bottlenecks suppress the lateral propagation of charge and contribute to defining the overall shape of the charge distribution in the arrays. Furthermore, variable topography and inter-NC spacing can lead to current flow patterns quite different from those predicted assuming a uniform film. Because small thickness variations by one monolayer can have a large effect as the two-dimensional limit is approached, this may further explain the apparent absence²⁵ so far of simple or universal transport scaling laws with film thickness and device size in drop-cast NC films. Though there

are other important factors governing charge transport in these systems, such as charge traps and array disorder, the restriction of transport by monolayers is an important factor that must be addressed in future designs of electronic devices based on NCs.

Acknowledgment. This work was supported partially by ONR (YIP N000140410489) and NSF (NSF Career Award DMR-0449533 and NSF NSEC DMR-0425780). We also gratefully acknowledge partial support from the NSF through the UPenn MRSEC program, DMR-0520020, including the use of its shared facilities.

Supporting Information Available. AFM and EFM scans of the electrode pair prior to PbSe nanocrystal deposition, AFM and EFM scans after PbSe nanocrystal deposition but before the *in situ* vacuum-annealing, EFM scans of the annealed NC array showing EFM signal evolution for a range of electric fields applied, AFM and EFM scans of another electrode pair on the same chip surface showing a similarly branched structure in the topography and EFM signals, AFM, EFM, and TEM scans of another sample with a different, parallel-plate electrode geometry containing highly ordered superlattice domains showing efficient electrical coupling of superlattices to the electrodes, efficient transport through domain boundaries, and an example of a conduction bottleneck, zoomed-in high-resolution TEM image of a single PbSe nanocrystal on the chip surface after *in situ* annealing in the AFM chamber showing a high degree of crystallinity. This material is available free of charge via the Internet at <http://pubs.acs.org>.

REFERENCES AND NOTES

- (1) Ashcroft; N. W. Mermin, N. D. *Solid State Physics*, 1st ed.; Holt, Reinhart and Winston: New York, 1976.
- (2) Alivisatos, P. *Science* **1996**, 271, 933.
- (3) Klimov, V. *Semiconductor and metal nanocrystals: Synthesis and electronic and optical properties*, 1st ed.; CRC Press: Boca Raton, FL, 2004.
- (4) Drndic, M.; Jarosz, M. V.; Morgan, N. Y.; Kastner, M. A.; Bawendi, M. G. *J. Appl. Phys.* **2002**, 92, 7498.
- (5) Mentzel, T. S.; Porter, V. J.; Geyer, S.; MacLean, K.; Bawendi, M. G.; Kastner, M. A. *Phys. Rev. B* **2008**, 77, No. 075316.
- (6) Hu, Z.; Fischbein, M. D.; Drndic, M. *Nano Lett.* **2005**, 5, 1463.
- (7) Talapin, D. V.; Murray, C. B. *Science* **2005**, 310, 5745–86.
- (8) Shim, M.; Guyot-Sionnest, P. *Nature* **2000**, 407, 981.
- (9) Yu, D.; Wang, C. J.; Wehrenberg, B. L.; Guyot-Sionnest, P. *Phys. Rev. Lett.* **2004**, 92, 216802.
- (10) Yu, D.; Wehrenberg, B. L.; Jhu, P.; Ma, J.; Guyot-Sionnest, P. *J. Appl. Phys.* **2006**, 99, 10435.
- (11) Porter, V. J.; Geyer, S.; Halpert, J. E.; Kastner, M. A.; Bawendi, M. G. *J. Phys. Chem. C* **2008**, 112, 2308.
- (12) Fischbein, M. D.; Drndic, M. *Appl. Phys. Lett.* **2005**, 86, 193106.
- (13) Jarosz, M. V.; Porter, V. J.; Fisher, B. R.; Kastner, M. A.; Bawendi, M. G. *Phys. Rev. B* **2004**, 70, 195327.
- (14) Lifshitz, E.; Brumer, M.; Kigel, A.; Sashchiuk, A.; Bashouti, M.; Sirota, M.; Galun, E.; Burshtein, Z.; Le Quang, A. Q.; Ledoux-Rak, I.; Zyss, J. *J. Phys. Chem. B* **2006**, 110, 25356.
- (15) Willis, L. J.; Fairfield, J. A.; Dadash, T.; Fischbein, M. D.; Drndic, M. *Nano Lett.* **2009**, 9, 4191.
- (16) Williams, K. J.; Tisdale, W. A.; Leschkies, K. S.; Haugstad, G.; Norris, D. J.; Aydil, E. S.; Zhu, X. Y. *ACS Nano* **2009**, 3, 1532.
- (17) Kang, M. S.; Lee, J.; Norris, D. J.; Frisbie, C. D. *Nano Lett.* **2009**, 9, 3848.
- (18) Law, M.; Luther, J. M.; Song, Q.; Hughes, B. K.; Perkins, C. J.; Nozik, A. J. *J. Am. Chem. Soc.* **2008**, 130, 5974.
- (19) Luther, J. M.; Law, M.; Song, Q.; Perkins, C. J.; Beard, M. C.; Nozik, A. J. *ACS Nano* **2008**, 2, 271.
- (20) Murphy, J. E.; Beard, M. C.; Nozik, A. J. *J. Phys. Chem. B* **2006**, 110, 25455.
- (21) Novikov, D. S.; Drndic, M.; Levitov, L. S.; Kastner, M. A.; Jarosz, M. V.; Bawendi, M. G. *Phys. Rev. B* **2005**, 72, No. 075309.
- (22) Coe, S.; Woo, W.-K.; Bawendi, M.; Bulovic, V. *Nature* **2002**, 420, 800.
- (23) Morgan, N. Y.; Leatherdale, C. A.; Drndic, M.; Jarosz, M. V.; Kastner, M. A.; Bawendi, M. *Phys. Rev. B* **2002**, 66, No. 075339.
- (24) Liljeroth, P.; Overgaag, K.; Urbina, A.; Grandidier, B.; Hickey, S. G.; Vanmaekelbergh, D. *Phys. Rev. Lett.* **2006**, 97, No. 096803.
- (25) Jdir, L.; Overgaag, K.; Gerritsen, J.; Vanmaekelbergh, D.; Liljeroth, P.; Speller, S. *Nano Lett.* **2008**, 8, 4014.
- (26) Drndic, M.; Markov, R.; Jarosz, M. V.; Bawendi, M. G.; Kastner, M. A.; Markovic, N.; Tinkham, M. *Appl. Phys. Lett.* **2003**, 83, 4008.
- (27) Martin, Y.; Abraham, D. W.; Wickramasinghe, H. K. *Appl. Phys. Lett.* **1988**, 52, 1103.
- (28) Viswanathan, R.; Heaney, M. B. *Phys. Rev. Lett.* **1995**, 75, 4433.
- (29) Cherniavskaya, O.; Chen, L.; Weng, V.; Yuditsky, L.; Brus, L. E. J. *Phys. Chem. B* **2003**, 107, 1525.
- (30) Bonnell, D. A.; Huey, B. L. In *Scanning Probe Microscopy and Spectroscopy, Theory, Techniques and Applications*, 2nd ed.; John Wiley and Sons: New York, 2001; pp 205–251.
- (31) Marchi, F.; Dianoux, R.; Smilde, H. J. H.; Mur, P.; Comin, F.; Chevrier, J. *J. Electrostatics* **2008**, 66, 538.
- (32) Fischbein, M. D.; Drndic, M. *Appl. Phys. Lett.* **2006**, 88, No. 063116.
- (33) Ginger, D. S.; Greenham, N. C. *J. Appl. Phys.* **2000**, 87, 1361.
- (34) Rabani, E.; Reichman, D. R.; Geissler, P. L.; Brus, L. E. *Nature* **2003**, 426, 271.